ADVANCED MATERIALS INTERFACES
www.advmatinterfaces.de

Chemical Sensing with Atomically Thin Platinum Templated by a 2D Insulator

*Kyung Ho Kim, Hans He, Marius Rodner, Rositsa Yakimova, Karin Larsson, Marten Piantek, David Serrate, Alexei Zakharov, Sergey Kubatkin, Jens Eriksson, and Samuel Lara-Avila**

Boosting the sensitivity of solid-state gas sensors by incorporating nanostructured materials as the active sensing element can be complicated by interfacial effects. Interfaces at nanoparticles, grains, or contacts may result in nonlinear current–voltage response, high electrical resistance, and ultimately, electric noise that limits the sensor read-out. This work reports the possibility to prepare nominally one atom thin, electrically continuous platinum layers by physical vapor deposition on the carbon zero layer (also known as the buffer layer) grown epitaxially on silicon carbide. With a 3–4 Å thin Pt layer, the electrical conductivity of the metal is strongly modulated when interacting with chemical analytes, due to charges being transferred to/from Pt. The strong interaction with chemical species, together with the scalability of the material, enables the fabrication of chemiresistor devices for electrical read-out of chemical species with sub part-per-billion (ppb) detection limits. The 2D system formed by atomically thin Pt on the carbon zero layer on SiC opens up a route for resilient and high sensitivity chemical detection, and can be the path for designing new heterogenous catalysts with superior activity and selectivity.

Chemiresistors represent a major class of commercial solid-state gas detectors due to ease of fabrication, simple operation, low cost, and possibility of miniaturization.[1–3] In these transducers, physicochemical interactions of the sensing material with gases can be simply monitored by a two-terminal resistance read-out.[4,5] With the advent of graphene, its use as chemical sensing element has led to outstanding sensitivities.[6] But while graphene is an exquisite charge sensor, it is a rather chemically inert material. Graphene's ability to interact with chemical species largely depends on its surface being functionalized with a sensitizing layer, such as metal/oxide nanoparticles,[7–9] or even polymeric residues from the microfabrication process.[6,10] Yet, chemical bonds to graphene that might occur during functionalization—or operation at high temperature in the functionalized material—can disrupt its transduction capabilities. In atomically thin crystals, covalent interaction with the crystal lattice can profoundly modify the band structure of the material, altering its electronic properties and with this, its charge sensing capabilities. This fragility toward chemical interactions of graphene, and 2D crystals in general, might compromise taking full

---

Dr. K. H. Kim, H. He, Prof. S. Kubatkin, Dr. S. Lara-Avila
Department of Microtechnology and Nanoscience
Chalmers University of Technology
Gothenburg SE-412 96, Sweden
E-mail: samuel.lara@chalmers.se

M. Rodner, Prof. R. Yakimova, Dr. J. Eriksson
Department of Physics
Chemistry and Biology
Linköping University
Linköping S-581 83, Sweden

Prof. K. Larsson
Department of Chemistry
Angstrom Laboratory
University of Uppsala
Box 538, Uppsala 75121, Sweden

The ORCID identification number(s) for the author(s) of this article can be found under https://doi.org/10.1002/admi.201902104.

DOI: 10.1002/admi.201902104

Dr. M. Piantek
Instituto de Nanociencia de Aragón and Laboratorio de Microscopías Avanzadas
Universidad de Zaragoza
Zaragoza 50018, Spain

Dr. M. Piantek, Dr. D. Serrate
Departamento de Física de la Materia Condensada
University of Zaragoza
Zaragoza 50009, Spain

Dr. D. Serrate
Instituto de Ciencia de Materiales de Aragón
CSIC
University of Zaragoza
Zaragoza 50009, Spain

Dr. A. Zakharov
MAX IV Laboratory
Lund 22100, Sweden

Dr. S. Lara-Avila
National Physical Laboratory
Hampton Road, Teddington TW11 0LW, UK

advantage of such prospective materials in emerging chemical sensing applications.[8,11,12]

The chemical-to-electrical transduction with atomically thin platinum presented here is based on inherent interactions of transition metals with chemical analytes, and the capability of preparing Pt in ultra-thin form, such that the resistance of the bulk-less metal is strongly dominated by surface effects. Thus, Pt acts simultaneously as the sensing and charge transducer layer. The possibility to prepare atomically thin Pt layers is enabled when the substrate for metal deposition, the so-called carbon zero layer (also known as buffer layer), is grown epitaxially on SiC (**Figure 1**a). In contrast to other substrates,[13–15] the insulating carbon zero layer is not only key to enable the 2D growth mode of Pt, but also to electrically probe the onset of conductivity of the surface at very early stages of Pt deposition, when the Pt layers are most sensitive to the chemical environment.

Figure 1b shows the current–voltage characteristic measured in situ, as Pt deposition takes place at a slow rate ($r = 0.017$ Å s^{-1}), on a 7×7 mm^2 substrate held at room temperature. The initial high resistance measured on the zero layer ($R >> 10$ GOhm) turns abruptly to an *ohmic*, linear current–voltage response after deposition of merely 2 Å of Pt (for the complete R vs thickness, see Figure S1, Supporting Information). The electrical resistance of Pt is particularly sensitive to the environment when the nominally deposited Pt thickness is $t \lesssim 1$ nm. For instance, Figure 1c shows the resistance changes of a nominally 3 Å thick

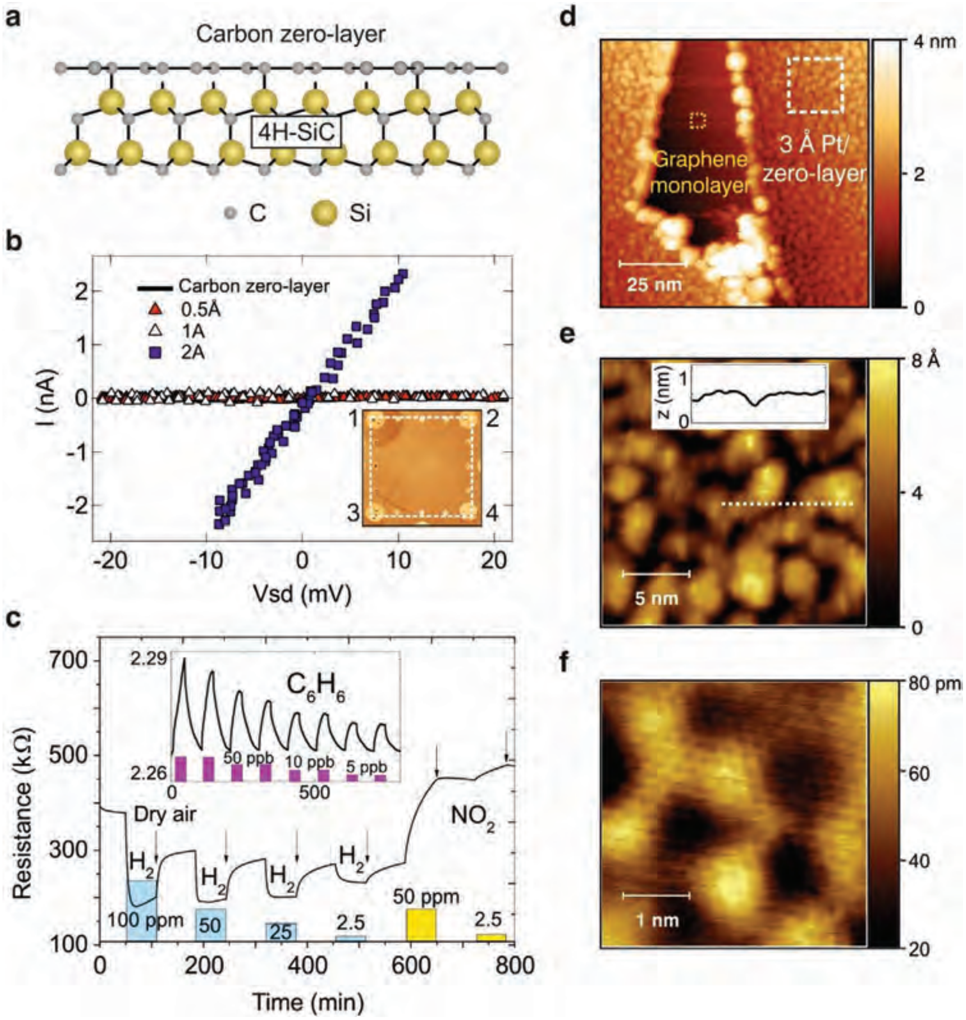

Figure 1. Atomically thin Pt as gas sensor. a) Schematic of the carbon zero layer, epitaxially grown on the silicon terminated face (0001) of 4H-SiC. b) Current–voltage characteristic measured in situ during Pt evaporation on a substrate at room temperature and nominal deposition rate $r = 1$ Å min^{-1} (background pressure $P = 5 \times 10^{-7}$ mbar). Inset: optical micrograph of the 7×7 mm^2 chip used for in situ resistance measurements; the resistance is measured between predeposited Pd contacts (circles) 1–2 and 3–4. Pt is deposited through a shadow mask with geometry indicated by the dashed white square. c) Sensing response of a 7 mm × 7 mm substrate under exposure to H_2, NO_2, and C_6H_6 (inset) in a background of dry air. Arrows indicate the time at which the gas test chamber is purged with dry air. For the inset, the baseline has been subtracted to compensate for linear drift. d) Constant current topography obtained by STM, giving an overview on a 100 nm × 100 nm area ($V_{STM} = 1$ V and $I_{STM} = 60$ pA) of the Pt covered surface in the neighborhood of a graphene monolayer inclusion. e) STM scan (20 nm × 20 nm, $V_{STM} = -200$ mV and $I_{STM} = 200$ pA) taken over a terrace (dashed white rectangle in (d)) showing the detailed topography of the Pt film. Inset: line profile indicated by the dotted line. f) STM scan ($V_{STM} = 200$ mV and $I_{STM} = 200$ pA) on the graphene monolayer inclusion showing that the graphene surface remains atomically clean after Pt deposition. The characteristic Moiré pattern of epitaxial graphene on SiC is evident in this atomically resolved scan.

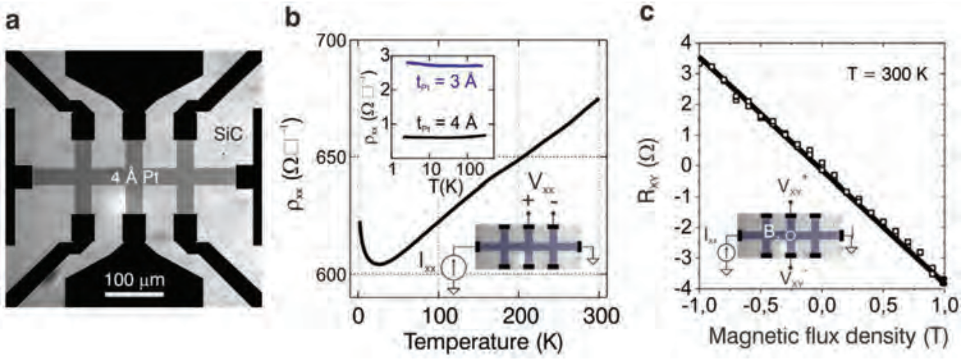

Figure 2. Electrical characterization of atomically thin Pt deposited on the carbon zero layer. a) Optical micrograph in light-transmission mode[16] of a Hall bar device ($L = 180$ µm × $W = 30$ µm) patterned on a nominally 4 Å thick Pt film. b) Temperature dependence of the longitudinal resistivity $\rho_{xx} = \frac{R_{XX}}{(L/W)} = \left(\frac{W}{L}\right)\left(\frac{V_{XX}}{I_{XX}}\right)$ measured on the device shown in (a). The device resistance decreases down to $T = 20$ K. The increase of resistance for $T < 20$ K is due to quantum corrections to the classical resistance.[17] Inset: comparison of temperature dependence of resistivity for 3 and 4 Å thick Pt films. c) Hall resistance $R_{XY} = V_{XY}/I_{XX}$ as a function of magnetic field B reveals a negative Hall coefficient $R_H = dR_{XY}/dB = -3.75$ Ω T^{-1}, signaling a hole-type conductivity in Pt with a carrier density $p = 1/(eR_H) = 1.77 \times 10^{14}$ holes cm^{-2} for this device.

Pt layer during exposure to standard test gases in the part-per-million range for strongly reducing (H_2) and strongly oxidizing (NO_2) gases. The inset of Figure 1c also shows that electrical detection of chemical species with atomically thin Pt is readily possible in the part-per-billion range, using benzene as example (for formaldehyde, see Figure S2, Supporting Information).

The surface of the Pt chemical transducer layer was investigated by combining scanning tunneling microscopy (STM) and electron transport measurements. Figure 1d shows a 100 × 100 nm^2 STM image of the substrate surface after deposition of 3 Å Pt. This particular STM scan shows, in addition to the Pt-decorated zero layer, a graphene monolayer inclusion which is a sub-product of the carbon zero-layer growth (for a larger STM scan, see Figure S3, Supporting Information). On the zero-layer area, we observe that Pt forms a coalescing network of islands, about 3 Å high and predominantly 2D in character (Figure 1e and inset therein). In sharp contrast, the surface of the graphene inclusion remains atomically clean after Pt deposition (Figure 1f), revealing the stronger adhesion of Pt to the carbon zero layer compared to that on graphene.

Electrical transport measurements on Hall bar devices made with atomically thin Pt, shown in **Figure 2**a, complement the scanning probe studies. First, the *metallic* resistance ($dR/dT > 0$) down to $T \approx 20$ K, shown in Figure 2b, implies that the Pt clusters observed by STM form a truly electrically interconnected network. Second, measurements in magnetic field (Figure 2c) revealed that atomically thin Pt is a hole-type conductor with a 2D hole density in the range $p_0 = 1\text{–}3 \times 10^{14}$ cm^{-2}, indicating carrier-asymmetric scattering at metal boundaries in this network.[18–20] Moreover, electrical characterization allows us to find the optimal conditions for the deposition, i.e., those yielding surfaces with the lowest resistance for a given Pt thickness. We found that a substrate temperature in the range 180–200 °C and a much faster deposition rate ($r = 1$ Å s^{-1}) reproducibly yield resistivity in the range $\rho \approx 1\text{–}3$ kΩ square^{-1} for $t = 3$ Å ($\rho \lesssim 1$ kΩ square^{-1} for $t = 4$ Å) and the Pt morphology shown in Figure 1e. The influence of the deposition parameters on the electrical resistance of atomically thin Pt highlights the role of kinetic effects on the early stages of Pt growth on the zero layer.

The carbon zero layer is the crucial ingredient to ensure the early onset of electrical conductivity of Pt at low coverage (see control experiments on other substrates in Figure S4, Supporting Information). The carbon zero layer is a highly ordered surface reconstruction of SiC resulting from thermal annealing at high temperature. If prepared properly, the zero layer is truly a 2D crystal, graphene-like, in which about 30% of the carbon atoms are chemically bound to the SiC substrate. The partial chemical bonding to SiC prevents the development of linear π-bands in the zero layer, rendering it electrically insulating.[21–23] The crystalline structure of the carbon zero layer was studied by low energy electron microscopy (LEEM), on substrates that led to low Pt sheet resistances (≈1 kΩ square^{-1}). For LEEM studies, Pt was deposited only on half of the chip through a shadow mask so as to allow the comparison between the Pt-free and the Pt-covered zero layer on the same substrate. The LEEM analysis shows that the Pt-free, pristine zero layer displays a clear contrast between two types of domains, marked with yellow and blue circles in **Figure 3**a. Micro-low energy electron diffraction (µ-LEED), shown in Figure 3b,c, revealed that this contrast arises from the presence of two different rotated crystal domains corresponding each to the $6\sqrt{3} \times 6\sqrt{3}$ carbon-rich phase of the zero layer (for Pt on the Si-rich SiC substrate, see Figure S5, Supporting Information).[22] In contrast, the Pt-covered area remains dark in LEEM across domains on the zero layer, independently of electron energy, due to the lack of the long-range order of the Pt layer. This lack of long-range order in Pt, observed from LEEM, is consistent with our STM studies (Figure 1d,e).

Density functional theory (DFT) calculations provide an insight on the origin of the quasi-2D growth mode of Pt on the zero layer that allows us to achieve an atomically thin metallic transducer. While kinetic constrains appear to determine the onset of electrical conductivity at low Pt coverage, the likelihood of a metal to wet the surface is ultimately given by thermodynamic considerations. At thermodynamic equilibrium, wetting is expected if the metal–substrate interfacial energy is lower than the difference between the surface free energy of the clean substrate and that of a clean metal.[24] With experimental surface free energy data not available for the zero layer, DFT has

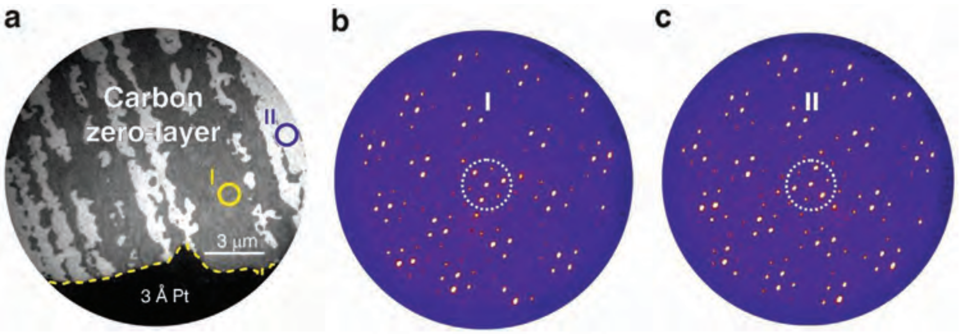

Figure 3. Surface characterization of atomically thin platinum deposited on the carbon zero layer. a) Bright-field low energy electron microscopy (LEEM) image of the substrate taken at the boundary (dashed line) between the bare carbon zero layer and the Pt-covered zero layer. The Pt-covered surface (bottom part of the image) appears dark at all electron energies due to the lack of long-range order in the Pt layer. The contrast observed on the zero layer (top part of the image), e.g., between the areas marked with yellow and blue circles in regions I and II, shows the presence of different zero-layer domains. b,c) Micro-low energy electron diffraction (LEED) images ($E = 48$ eV, sampling area 500 nm) collected on the zero layer from regions I (yellow) and II (blue) in (a), respectively, reveal that the LEEM contrast arises from the presence of two different rotated crystal domains (highlighted by the dashed white circle).

provided the theoretical adhesion energies of Pt atoms on free-standing graphene (G), the $6\sqrt{3} \times 6\sqrt{3}$ carbon-rich zero layer on SiC (ZL/SiC), and graphene/ZL/SiC (G/SiC) substrates. The adhesion energies are defined as $\Delta E_{\text{adhesion}} = E_{\text{surface-Pt}} - E_{\text{surface}} - E_{\text{Pt}}$, with $E_{\text{surface-Pt}}$ corresponding to Pt atoms bound to the surface, E_{surface}, the energy for the radical surface before Pt binding, and E_{Pt}, the energy of Pt atoms in vacuum. Among the studied surfaces, it was found that the strongest binding for Pt atoms occurs when the substrate is the zero layer on the SiC surface and weakest on a free-standing graphene. Using clusters composed of up to 32 atoms of Pt, the adhesion strengths per Pt atom on the zero layer is with $\Delta E^{\text{32Pt}-\text{ZL/SiC}}_{\text{adsorbtion}} = -3.1$ eV roughly an order of magnitude larger compared to that of Pt to free-standing graphene ($\Delta E^{\text{32Pt}-\text{G}}_{\text{adsorbtion}} = 0-.2\text{eV}$) (see Figure S6 and Table S1 in the Supporting Information for DFT results). The resulting stable conformation for the large Pt cluster on the carbon zero layer is shown in **Figure 4**a. Overall, the reason of the enhanced affinity of the Pt atoms to the zero layer is the presence of carbon atoms bound to the SiC surface, which have lost their sp^2 character and are thereby very reactive, making the wetting of zero layer by Pt a thermodynamically favorable process.

Having discussed the formation and electrical properties of atomically thin Pt on the carbon zero layer, the charge-transfer sensing mechanism was investigated through the response (resistive read-out) of chemiresistors devices (see Figure S7, Supporting Information) to benzene, for which the interaction with Pt is well known.[25,26] Figure 4b shows the normalized resistance $\hat{R} = \Delta R / R_0 = (R - R_0)/R_0$ of a device exposed to benzene diluted in nitrogen, with R the device resistance during gas exposure and R_0 the baseline resistance before exposure. The decrease of the electrical resistance of Pt chemiresistors upon exposure to benzene, shown in Figure 4b, can be explained through the effect of excess charges on the classical conductivity of the metal. Justified by our (magneto) transport measurements (Figure 2b,c), we consider the single-band approximation of the Drude conductivity of platinum $\sigma_{\text{Pt}} = |e| p \mu$, with e the elementary charge, p the hole carrier density, and μ the carrier mobility. Assuming that the benzene adsorbed on the Pt surface does not significantly modify the mobility μ of carriers in the metallic network,[27] fluctuations in the conductivity of Pt would be the consequence of changes in carrier density. Our DFT calculations point in this direction (for details, see Figure S8, Supporting Information). Figure 4c shows geometrically optimized benzene on Pt, stabilized by Van der Waals interactions, which yield a net hole transfer of $0.14|e|$ from the benzene molecule to Pt. This corresponds to a charge transfer density of about $\Delta p_{\text{C6H6}} \approx 5 \times 10^{13}$ holes cm^{-2}, which is comparable in magnitude and carrier type to the measured baseline carrier density of Pt, $p_0 = 1\text{–}3 \times 10^{14}$ cm^{-2} (Figure 2c). This increase in hole carrier density, $p_0 + \Delta p_{\text{C6H6}}$, allows us to qualitatively explain the decrease of resistance in Pt when it interacts with benzene.

The measurements on chemiresistor devices exposed to benzene also shed light upon the detection limits using atomically thin Pt as sensing layers in quasi-realistic operational conditions, i.e., in a background of artificial air. Figure 4d shows the concentration-dependent response from 100 ppb down to 5 ppb, the lowest concentration attainable in our setup. Note that measurements in dry air invert the sensor response compared to measurements performed in pure N_2 (Figure 4b). This resistance increase upon benzene/air exposure can be the result of oxygen/benzene competition over adsorption sites and/or through reactions with adsorbed O^-.[28] In these experimental conditions, the raw response time (time to reach 90% of steady state) is $t_r \approx 24$ min for 5 ppb. Alternatively, t_r can be evaluated based on the initial resistance increment rate, dR/dt, during gas exposure.[29,30] Defining t_r as the time when dR/dt reaches the maximum value during exposure, we find $t_r \approx 12$ s for 5 ppb of benzene. Now, the ultimate detection limit for benzene is estimated by considering the response of $\Delta R = 47\ \Omega$ at 5 ppb, and assuming a linear sensitivity in the range 0–5 ppb. With an effective noise floor in our setup of 1.9 Ω at the operating temperature ($T = 100$ °C), the extrapolated lower detection limit for benzene is of the order of $1.9\ \Omega/(47\ \Omega/5\ \text{ppb}) = 210$ part-per-trillion. Given the charge transfer sensing mechanism, the sensitivity is higher for more strongly reducing/oxidizing gases as seen in the relative response $\text{rr} = \Delta R_{\text{sat}}/R_0 = (R_{\text{sat}} - R_0)/R_0$ in Figure 4e, with R_{sat} the saturated resistance after gas exposure. The linear sensor response in the range 100–5 ppb yields a sensitivity of ≈0.2% ppb^{-1} to NO_2 (at $T = 200$ °C), roughly 50 times higher than that to benzene. The sensors work without degradation for more than 2 years if the operating temperature is kept at 150 °C or lower. For temperatures above 200 °C, the resistance of the sensors changes permanently, which we

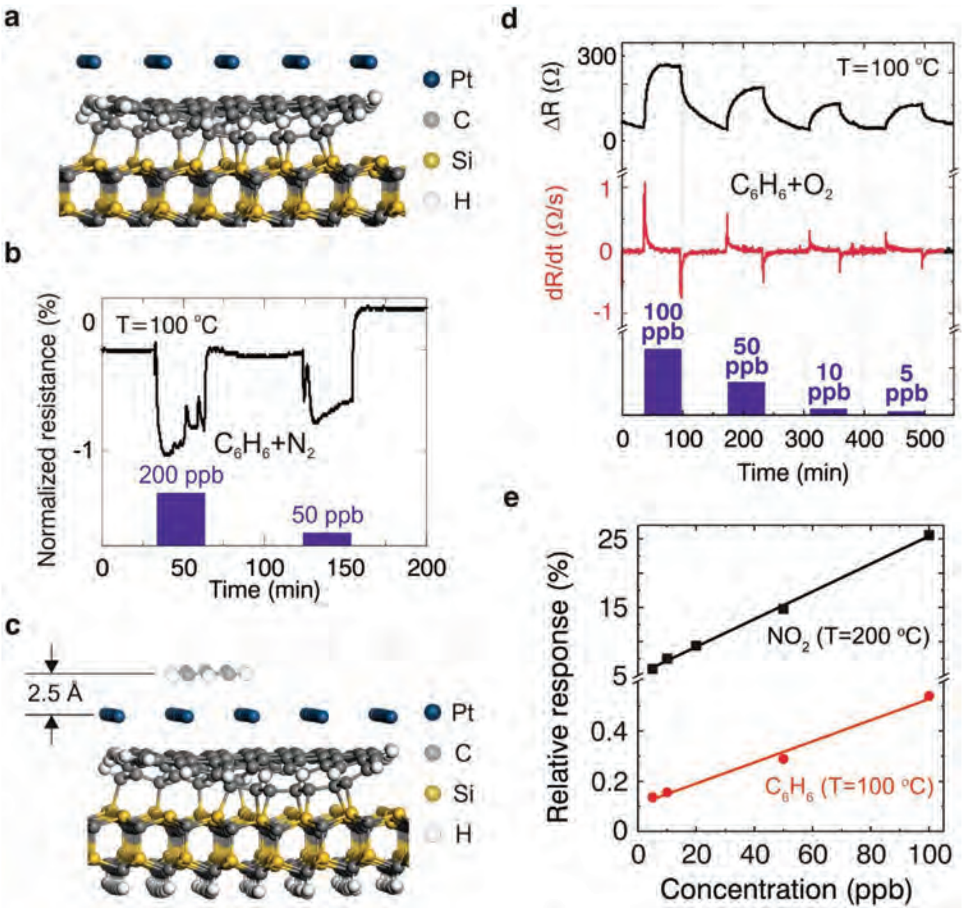

Figure 4. Chemical to electrical transduction with atomically thin Pt. a) The interfacial slab is the relaxed geometry obtained from DFT calculations of a Pt monolayer on the zero layer, partially binding to a SiC surface. For calculations, the outer carbon atoms in the zero layer are H-terminated. In our calculations, all surfaces were geometrically relaxed before the adhesion of Pt took place. b) Resistive read-out signal from atomically thin Pt chemiresistor in response to benzene in N_2 background shown as the normalized resistance, $\hat{R} = \Delta R/R_0 = (R - R_0)/R_0$, with R the device resistance during gas exposure and $R_0 \approx 20\ \Omega$ the baseline resistance before exposure. For these measurements, the temperature is $T = 100$ °C. c) DFT calculations help to explain the benzene detection mechanism shown in (b). This image is an interfacial slab of a geometrically relaxed benzene molecule physisorbed on the Pt surface. The most stable conformation of benzene on Pt is that of benzene lying flat on the surface. With an equilibrium benzene–Pt distance of 2.5 Å, the adhesion strength of 0.10 eV is in the range of Van der Waals interactions and we find a hole transfer of $0.14|e|$ from the benzene molecule to Pt. d) Response to benzene concentrations in the range from 5 to 100 ppb at $T = 100$ °C of a large-area device (5 mm × 5 mm). The black line shows the changes in device resistance upon exposure to benzene, $\Delta R = (R - R_0)$ with $R_0 \approx 39$ kΩ, and the red line is its first-order time derivative. e) Comparison of the concentration-dependent relative response $\Delta R_{sat}/R_0 = (R_{sat} - R_0)/R_0$, with R_{sat} the saturated resistance after gas exposure, for NO_2 ($T = 200$ °C) and C_6H_6 ($T = 100$ °C).

attribute to microscopic changes in the atomically thin metal layer. Only the results corresponding to the operating conditions yielding the best performance for the individual gases are reported here.

Finally, in addition to platinum, it was found that atomically thin palladium deposited on the carbon zero-layer surface (see Figure S9, Supporting Information) also results in an electrically conductive surface, sensitive to the chemical environment. The well-ordered zero layer on SiC could thus be a suitable support for the deposition of metals that have similar chemistry as the Pt and Pd systems.[15,24] The demonstrated gas sensing performance with atomically thin Pt proof-of-concept devices at relatively low temperature ($T = 100$ °C), coupled with gas discrimination techniques,[31] could already allow fast, sensitive, and selective detection of extremely toxic molecules at concentrations of relevance to, for instance, air quality monitoring. Atomically thin metals as a new platform for gas detection, aided with surface science studies, could facilitate research aiming at tuning the selectivity of gas sensing devices operating at room temperature, requirements which have proven to be challenging to meet in solid-state gas detectors. Furthermore, the carbon zero layer, which enables the possibility to template atomically thin metals, may also serve as a platform for epitaxy of other 2D materials and the design of new heterogenous catalyst with superior activity and selectivity for challenging reactions.[32]

Experimental Section

Growth of Carbon Zero Layer on SiC: The carbon zero layer is an integral part of the epitaxial graphene-SiC material system and is the first to form when the SiC substrate is exposed to high temperature

($T > 1500$ °C). More specifically, this is the carbon-rich surface reconstruction ($6\sqrt{3} \times 6\sqrt{3}$) characteristic of Si face SiC at elevated temperatures. To prevent the growth of graphene and grow only the carbon zero layer, here 7×7 mm^2 4H-SiC substrates were used and a gradual (inductive) heating in argon atmosphere was applied until $T \approx 1700$ °C was reached and that was kept for 30 s. Then the furnace was switched off and the samples were taken out at room temperature. Prior to growth, the chamber was pumped down to a base pressure of $P_0 = 1 \times 10^{-6}$ mbar in order to minimize oxygen contamination which is detrimental for a complete carbonization.

Metal Deposition: Metals were deposited by e-beam evaporation at base pressure $P_0 = 5 \times 10^{-7}$ mbar in a Lesker PVD 225 fitted with a custom-built substrate heater. Before metal deposition, the substrate temperature was raised (e.g., to 180–200 °C) and kept constant for 5 min. The deposition rate could be adjusted reliably down to $r = 0.017$ Å s^{-1}, setting the minimum rate used in these experiments. A rate of r = 1 Å s^{-1} yielded the most conductive metal layer for a given thickness.

Scanning Tunneling Microscopy: STM characterization was performed in an Aahrus STM operated at room temperature and at a base pressure of 1×10^{-10} mbar. The tip was an etched W wire attached to the resonator of a Kolibri sensor, and this work was done under sample bias convention.

Microfabrication: Patterning of the conductive layers into diverse geometries including Hall bars (30 µm × 180 µm), square bridges, and interdigitated fingers, was done by two-step electron beam lithography. In the first lithography, Pd (100 nm) contacts were defined on top of the conductive layers and boundaries of the devices were carved out by reactive ion dry etching in NF_3 gas using poly(methyl methacrylate) resists as a mask in the second lithography. Lithography-free chemiresistor sensor devices were fabricated through deposition of Pd contacts on top of the Pt/zero layer/SiC substrates using a shadow mask that had square electrodes with a 1 mm gap in between.

Gas Sensing: After processing, the chip was mounted on a ceramic heater substrate (Heraues GmbH, Germany) along with a Pt100 temperature sensor using ceramic glue (Aremco Ceramabond 571). A single channel source measure unit (SMU, Keithley 2601 SourceMeter) was used to drive the sensor. The inter electrode resistance was recorded at 1 Hz. Gas exposure was controlled by a gas mixer system consisting of Bronkhorst mass flow controllers connected to PC-controlled sequencing software. Flow over the sensor was constant at 100 mL min^{-1}. The gas was kept at room temperature during all experiments. A dry background mixture of N_2 and O_2 with a ratio of 80:20 mL min^{-1} and a constant flow rate of 100 mL min^{-1} was used both as a carrier gas and purging gas. The nitrogen concentration was then adjusted when introducing test gases (NO_2, C_6H_6, CH_2O) to the gas flow. The sensor was exposed to test gas for 40 min toward 100, 50, 10, and 5 ppb, respectively, with 80 min of purging in a mixture of 20% dry oxygen in a background of nitrogen.

Density Functional Theory: The energetic stability and geometrical structure of a SiC/zero layer/Pt layer were investigated theoretically by performing DFT calculations under periodic boundary conditions. In addition, the reactivity of this layer for benzene molecules was also studied. More specifically, an ultrasoft pseudopotential plane-wave approach was used, based on the Perdew–Burke–Ernzerhof generalized gradient approximation (GGA) of the exchange–correlation functional.[33] The GGA took into account the gradient of the electron density, which gave a high-quality energy evaluation. To include Van der Waals interactions in the calculations, dispersion corrections were made for all calculations in the present study. Moreover, the value of the energy cutoff for the plane wave basis sets was set to 420.00 eV. In addition, the Monkhorst–Pack scheme was used for the *k*-point sampling of the Brillouin zone, which generated a uniform mesh of *k* points in reciprocal space.[34] All atoms within the interface region were allowed to move freely in the calculations by using a BFGS approach (Broyden–FletcherGoldfarb–Sharmo).[35] The calculations in the present work were carried out using the Cambridge Sequential Total Energy Package (CASTEP) program from BIOVIA, Inc.[36] The 4H-SiC (0001) surface was used in modeling the interfacial slab. The bottom layer atoms were terminated with H in order to saturate the dangling bonds and to simulate the continuation into the bulk. All atoms, except the two bottom atomic layers, were allowed to freely relax in a geometry optimization procedure. A graphene monolayer was thereafter added to the relaxed SiC surface. In order to reduce interfacial strengths, the graphene monolayer was constructed as a very large flake, where the edge carbons were saturated with hydrogen atoms. The resulting interfacial slab was again allowed to relax, which resulted in a carbon zero layer forming a buckled structure on the SiC surface. This theoretically obtained zero layer was covalently binding to the underlying Si surface atoms to 20%, which was very similar to the experimentally obtained zero layer. This final SiC/zero-layer slab was from here on used for the growth of a monolayer 2D Pt layer, and for the reaction between gaseous benzene and this Pt layer. The calculated adsorption strengths for a 9 and 32 Pt atoms cluster yielded the similar results. The reason to use a large flake and not a continuous 2D Pt sheet was the presence of large strains obtained for the latter situation.

For benzene, the benzene molecule was initially positioned i) parallel, ii) orthogonal, or iii) with an angle of 45° with respect to the surface. It was noted that for chemisorbed benzene, additionally, there was only one plausible sp^2-to-sp^3 transformation of a benzene C atom upon binding to Pt. This later however, was unstable, and as a result of geometry optimization became desorbed from the surface, returning to the physisorbed conformation where the benzene molecule lay flat on the Pt/zero-layer surfaces as in Figure 4c.

Supporting Information

Supporting Information is available from the Wiley Online Library or from the author.

Acknowledgements

The authors thank M. Skoglundh for instructive discussions, and A. Yurgens, J. F. Schneiderman, and A. Danilov for critical reading of the manuscript. S.L.A. thanks Mats Hagberg for assistance with in situ resistance measurements during Pt deposition. This work was jointly supported by the Swedish Foundation for Strategic Research (SSF) (nos. IS14-0053, GMT14-0077, RMA15-0024), Knut and Alice Wallenberg Foundation, Chalmers EI NANO, The Swedish Research Council (VR) 2015–03758, and The Swedish-Korean Basic Research Cooperative Program of The NRF (no. NRF-2017R1A2A1A18070721).

Conflict of Interest

The authors declare no conflict of interest.

Keywords

atomically thin materials, buffer layer, chemical sensors, nanomaterials

Received: December 13, 2019
Revised: March 18, 2020

---

[1] M. E. Franke, T. J. Koplin, U. Simon, *Small* **2006**, *2*, 36.
[2] D. R. Miller, S. A. Akbar, P. A. Morris, *Sens. Actuators, B* **2014**, *204*, 250.
[3] J. Zhang, X. Liu, G. Neri, N. Pinna, *Adv. Mater.* **2016**, *28*, 795.

[4] W. H. Brattain, J. Bardeen, *Bell Syst. Tech. J.* **1953**, *32*, 1.
[5] T. Seiyama, A. Kato, K. Fujishi, M. Nagatami, *Anal. Chem.* **1962**, *34*, 1502.
[6] F. Schedin, A. Geim, S. Morozov, E. Hill, P. Blake, M. Katsnelson, K. Novoselov, *Nat. Mater.* **2007**, *6*, 652.
[7] J. Yi, J. M. Lee, W. Il Park, *Sens. Actuators, B* **2011**, *155*, 264.
[8] W. Yuan, G. Shi, *J. Mater. Chem. A* **2013**, *1*, 10078.
[9] J. Eriksson, D. Puglisi, Y. H. Kang, R. Yakimova, A. Lloyd Spetz, *Phys. B* **2014**, *439*, 105.
[10] Y. Dan, Y. Lu, N. J. Kybert, Z. Luo, A. T. C. Johnson, *Nano Lett.* **2009**, *9*, 1472.
[11] S. Yang, C. Jiang, S. H. Wei, *Appl. Phys. Rev.* **2017**, *4*, 021304.
[12] C. Anichini, W. Czepa, D. Pakulski, A. Aliprandi, A. Ciesielski, P. Samorì, *Chem. Soc. Rev.* **2018**, *47*, 4860.
[13] J. S. Agustsson, U. B. Arnalds, A. S. Ingason, K. B. Gylfason, K. Johnsen, S. Olafsson, J. T. Gudmundsson, *Appl. Surf. Sci.* **2008**, *254*, 7356.
[14] S. Shimizu, K. S. Takahashi, T. Hatano, M. Kawasaki, Y. Tokura, Y. Iwasa, *Phys. Rev. Lett.* **2013**, *111*, 216803.
[15] A. I. Maaroof, B. L. Evans, *J. Appl. Phys.* **1994**, *76*, 1047.
[16] T. Yager, A. Lartsev, S. Mahashabde, S. Charpentier, D. Davidovikj, A. V Danilov, R. Yakimova, V. Panchal, O. Kazakova, A. Tzalenchuk, S. Lara-Avila, S. Kubatkin, *Nano Lett.* **2013**, *13*, 4217.
[17] G. Bergmann, *Phys. Rep.* **1984**, *107*, 1.
[18] L. R. Windmiller, J. B. Ketterson, S. Hornfeldt, *J. Appl. Phys.* **1969**, *40*, 1291.
[19] O. K. Andersen, *Phys. Rev. B* **1970**, *2*, 883.
[20] G. Fischer, H. Hoffmann, J. Vancea, *Phys. Rev. B* **1980**, *22*, 6065.
[21] S. Goler, C. Coletti, V. Piazza, P. Pingue, F. Colangelo, V. Pellegrini, K. V. Emtsev, S. Forti, U. Starke, F. Beltram, S. Heun, *Carbon* **2013**, *51*, 249.
[22] C. Riedl, U. Starke, J. Bernhardt, M. Franke, K. Heinz, *Phys. Rev. B* **2007**, *76*, 245406.
[23] M. S. Nevius, M. Conrad, F. Wang, A. Celis, M. N. Nair, A. Taleb-Ibrahimi, A. Tejeda, E. H. Conrad, *Phys. Rev. Lett.* **2015**, *115*, 136802.
[24] C. T. Campbell, *Surf. Sci. Rep.* **1997**, *27*, 1.
[25] M. C. Tsai, E. L. Muetterties, *J. Am. Chem. Soc.* **1982**, *104*, 2534.
[26] C. Morin, D. Simon, P. Sautet, *J. Phys. Chem. B* **2004**, *108*, 5653.
[27] A. Krokhin, N. Makarov, V. Yampol'skii, *Sov. Phys. - JETP* **1991**, *72*, 289.
[28] A. Dey, *Mater. Sci. Eng., B* **2018**, *229*, 206.
[29] M. Rodner, J. Bahonjic, M. Mathisen, R. Gunnarsson, S. Ekeroth, U. Helmersson, I. G. Ivanov, R. Yakimova, J. Eriksson, *Mater. Des.* **2018**, *153*, 153.
[30] C.-H. Wu, G.-J. Jiang, C.-C. Chiu, P. Chong, C.-C. Jeng, R.-J. Wu, J.-H. Chen, *Sens. Actuators, B* **2015**, *209*, 906.
[31] A. Schütze, N. Helwig, T. Schneider, *J. Sens. Sens. Syst.* **2018**, *7*, 359.
[32] Y. Liu, D. Gokcen, U. Bertocci, T. P. Moffat, *Science* **2012**, *338*, 1327.
[33] J. P. Perdew, K. Burke, M. Ernzerhof, *Phys. Rev. Lett.* **1996**, *77*, 3865.
[34] H. J. Monkhorst, J. D. Pack, *Phys. Rev. B* **1976**, *13*, 5188.
[35] T. Schlick, *Molecular Modeling and Simulation: An Interdisciplinary Guide*, Springer-Verlag, Berlin, Heidelberg **2002**.
[36] S. J. Clark, M. D. Segall, C. J. Pickard, P. J. Hasnip, M. I. J. Probert, K. Refson, M. C. Payne, *Z. Kristallogr.* **2005**, *220*, 567.